Tailoring Molecular-Scale Contact at Perovskite/Polymeric Hole Transporting Material Interface for Efficient Solar Cells

Jiaonan Sun[†], Ke Ma[†], Zih-Yu Lin, Yuanhao Tang, Dharini Varadharajan, Alexander X. Chen, Harindi R. Atapattu, Yoon Ho Lee, Ke Chen, Bryan W. Boudouris, Kenneth R. Graham, Darren J. Lipomi, Jianguo Mei, Brett M. Savoie*, Letian Dou**

Dr. J Sun, Dr. K Ma, Z.-Y. Lin, Y. Tang, D. Varadharajan, Dr. Y. H. Lee, Prof. B. W. Boudouris, Prof. B. M. Savoie, Prof. L. Dou

Davidson School of Chemical Engineering, Purdue University, West Lafayette, IN 47907, USA

E-mail: dou10@purdue.edu; bsavoie@purdue.edu;

A. X. Chen, Prof. D. J. Lipomi

Department of NanoEngineering, University of California, San Diego, La Jolla, CA 92093, USA

H. R. Atapattu, Prof. K. R. Graham

Department of Chemistry, University of Kentucky, Lexington, KY 40506, USA

K. Chen, Prof. J. Mei

Department of Chemistry, Purdue University, West Lafayette, IN 47907, USA

This article has been accepted for publication and undergone full peer review but has not been through the copyediting, typesetting, pagination and proofreading process, which may lead to differences between this version and the Version of Record. Please cite this article as doi: 10.1002/adma.202300647.

E-mail: jgmei@purdue.edu

Prof. L. Dou

Birck Nanotechnology Center, Purdue University, West Lafayette, IN 47907, USA

Keywords: perovskite solar cells, PTAA, 2D/3D heterostructure, interface engineering

Abstract: Perovskite solar cells (PSCs) have delivered more than 25% of power conversion efficiency (PCE) and incorporating polymers as hole transporting layers (HTLs) can further enhance the stability of devices towards the goal of commercialization. Among various polymeric hole transporting materials, poly(triaryl amine) (PTAA) is one of the promising HTL candidates with good stability; however, the hydrophobicity of PTAA causes problematic interfacial contact with perovskite, limiting the device performance. Using molecular side-chain engineering, we successfully constructed a uniform two-dimensional (2D) perovskite interlayer with conjugated ligands, between three-dimensional (3D) perovskites and PTAA. Further, employing conjugated ligands as cohesive elements, perovskite/PTAA interfacial adhesion was significantly improved. As a result, the thin and lateral extended 2D/3D heterostructure enabled the as-fabricated PTAA-based PSCs to achieve a PCE of 23.7%, improved from the 18% of reference devices. Owing to the increased ion migration energy barrier and conformal 2D coating, unencapsulated devices with the new ligands exhibited both superior thermal stability under 60°C heating and moisture stability in ambient conditions.

1. Introduction

Perovskite solar cells (PSCs) recorded over 25% power conversion efficiency (PCE)[1–6] but their limited stability still hinders the industrial path towards commercialization. Polymeric hole transporting layers (HTLs), especially poly(triaryl amine) (PTAA), have been adopted to improve the stability of devices. However, they have also resulted in a sacrifice on the device efficiency.[7–12] The main limitation of PTAA is its incompatibility with perovskite which impedes interfacial contact between perovskite and PTAA, thus inhibiting charge transfer at interfaces.[13–16] The construction of 2D/3D heterojunctions is an effective strategy to tackle these interfacial problems as they can

improve energy band alignment, enhance charge transfer and stabilize surface lattices.[8,17–22] Subsequently, the implementation of 2D/3D heterostructures in PSCs with polymeric HTL requires the synergistic roles of the 2D structures, as forming strong interactions with PTAA, while also constructing a good morphological contact between 2D and 3D perovskites. Despite many studies on 2D perovskite passivation,[23,24] less investigation has been done on controlling the spatial growth of 2D perovskite on 3D surface and the spatial heterogeneity of the 2D/3D heterostructure. Incorporating conjugated ligands into 2D/3D heterojunction has shown great promise in improving charge transfer at interfaces.[19,20] It also provides vast opportunities for increasing the intermolecular interactions with PTAA,[25–27] and for tailoring the 2D structures due to the rich tunability of molecular configurations and its influence on 2D crystal growth.

Herein, via a side-chain engineering approach, we developed a series of conjugated organic ligands, based on quaterthiophene skeletons, and incorporated them into PSCs with an architecture of glass/ITO/SnO_2/perovskite/ligands/PTAA/Au (**Figure 1**a). The designed ligands are composed of methyl, ethyl or di-methyl side chains on thiophene units, denoted as 4TmI, 4TeI, and 4TdmI, respectively (Figure 1b). When the bulky conjugated ligands are assembled on the 3D perovskite surface, the interface adhesion between PTAA and perovskite is enhanced by π-π interactions. We also observed the mesoscopic variations of growth dynamics and surface heterogeneity of 2D perovskite layers with different ligands, which can be correlated with the lattice strain and ligand solubility, induced by the differences in molecular configuration. With this understanding, solar cells fabricated with 4TeI and PTAA hole transporting layer were able to achieve over 23% PCE. Moreover, the as-fabricated device retains 80% of its initial efficiency for 1100 hours under heating at 60 °C in N_2 and 100% of its initial efficiency for 2640 hours in ambient condition without encapsulation.

2. Result and Discussion

2.1. Ligand synthesis and 2D perovskite properties

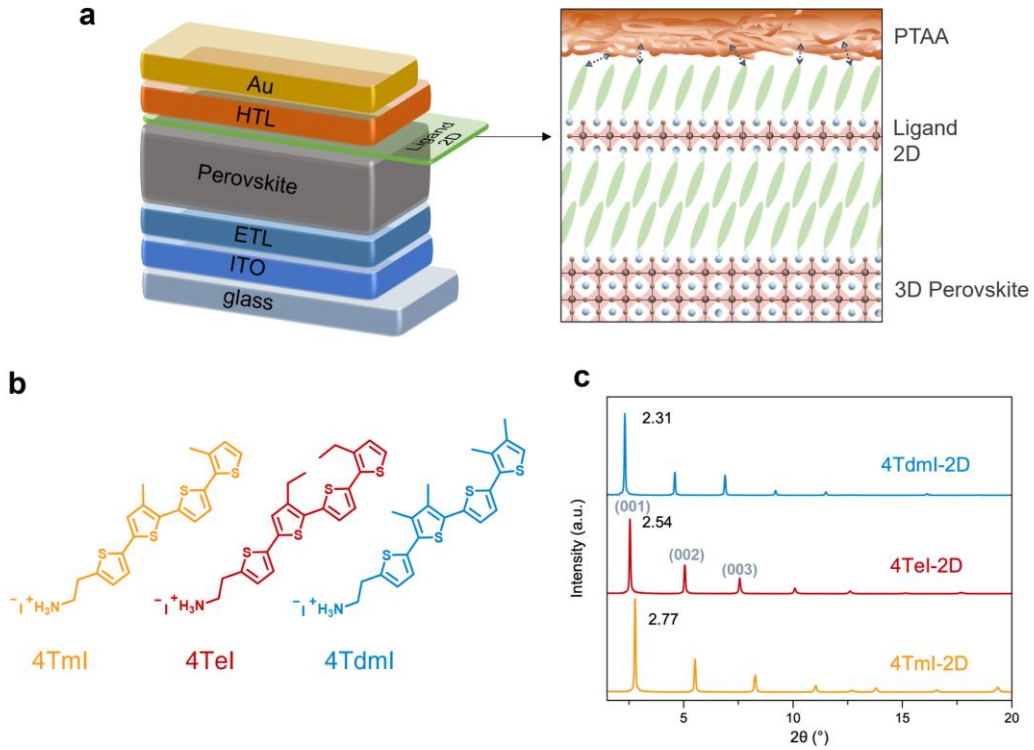

Figure 1. Ligand design for surface passivation a) Device architecture and perovskite/ligand/PTAA interface. b) Chemical structures of different ligands, named as 4TmI, 4TeI and 4TdmI. c) XRD of 2D perovskite thin films fabricated with different ligands.

The syntheses of 4TeI and 4TdmI started from 3-ethylthiophene and 3,4-dimethylthiophene, respectively, which were then extended to quaterthiophenes by Stille coupling reactions. In total, five reaction steps were carried out for each ligand and the final iodide salts obtained were of device-grade purity (Figure S1 and S2). To address the solubility issue of quaterthiophene ammonium iodide in non-polar solvents, which are orthogonal solvents of the underlying perovskites, and achieving uniform coating of 2D/3D heterojunction, methyl groups or ethyl groups were added onto the thiophene rings to induce distortion between thiophenes (Fig. 1b, 4TmI, 4TeI, and 4TdmI).[28] Ethyl groups, instead of methyl groups, allow further improvement in solubility due to the increased length of the aliphatic alkyl chains (Fig. 1b and S3, 4TeI). Interestingly, despite

having the exact same molecular formula with 4TeI, 4TdmI exhibits significantly decreased solubility (Fig. 1b and S3). Based on molecular dynamics (MD) simulation, 4TdmI exhibits stronger intermolecular interactions, thus leading to a slightly larger (less negative) solvation free energy (−36.2 kcal/mol), as compared to 4TeI (−37.8 kcal/mol) and 4TmI (−36.5 kcal/mol). These simulation results agree with the lower solubility of 4TdmI observed experimentally.

The 2D perovskite films incorporating 4TmI, 4TeI and 4TdmI exhibit different structural and electronic properties. We measured the X-ray diffraction (XRD) of 2D perovskite thin films prepared with mixed solutions of ligands and PbI_2, which showed layered structure patterns for all the samples with orientation parallel to substrates (Figure 1c). Based on the reflections located at 2.77°, 2.54° and 2.31°, we calculated the d-spacings of 4TmI, 4TeI, and 4TdmI 2D perovskite samples as 3.18 nm, 3.47 nm and 3.82 nm, respectively, which are different from the pure-ligand patterns (Figure S4). Interestingly, the side-chain modification of the conjugated ligands with same length significantly altered the out-of-plane interlayer distances, causing up to 0.6 nm differences. The increase of d-spacing in 4TeI and 4TdmI samples could be attributed to an increase in dihedral angle between the ligands and the horizontal inorganic plane, induced by the side-to-side bulkiness (Figure S5). Grazing-incidence wide-angle X-ray scattering was carried out to confirm the in-plane 2D perovskite structure from the Q_{xy} at ~1 $Å^{-1}$ (Figure S6). UV-vis absorption spectra featured sharp excitonic peaks at 520 nm (2.38 eV) for both 4TeI and 4TmI mixed with PbI_2 (Figure S7), which further confirmed the formation of n=1 Ruddlesden-Popper 2D perovskite phase. Conversely, a hypsochromic shift of the excitonic peak from 520 nm to 477 nm (2.6 eV) was observed for 4TdmI sample, accompanied with the yellow appearance of the thin film (different from a typical orange color of 2D n=1 perovskites). This result suggests that a strained 4TdmI 2D perovskite structure is formed and the absorbance shift could be induced by highly distorted inorganic $[PbI_6]^{4-}$ octahedra. To assess the potential of 2D perovskite as a hydrophobic protecting layer for 3D perovskite, the aqueous stability was investigated by directly immersing 2D perovskite thin films in water (Figure S8), and the film degradation was monitored by XRD and UV-vis spectroscopy. The 4TeI 2D perovskite thin films were stable up to 8 weeks, while 4TmI and 4TdmI 2D perovskite thin films degraded within a week and 3 days, respectively. The enhanced stability could be attributed to the bulkiness and hydrophobicity of the ethyl side chain on 4TeI, while the fast degradation of 4TdmI sample is likely due to the distorted

2D perovskite lattice. The excellent aqueous stability of 4TeI 2D perovskite shows its great potential for improving the moisture stability of PSCs through the formation of 2D/3D heterostructures. Additionally, the desired ligands are expected to form type-II energy alignment in 2D perovskite structure between organic and inorganic layers,[28] allowing more efficient out-of-plane charge transfer. Cyclic voltammogram shows similar oxidation potential for all ligand molecules indicating the side-chain modification does not significantly alter the energy levels (Figure S9), while PL quenching in 2D thin film formed with every ligand further confirmed type-II energy alignment (Figure S10).

2.2. Surface reconstruction of 2D/3D heterostructure

To evaluate the implication of the 2D structure in devices, we investigated the formation of 2D/3D heterostructures with different ligands. The solubilities of the ligands in solution and the ligand configurations directly affect the coverage of the ligands on 3D perovskite surface as well as the growth mechanism of the 2D/3D heterojunction. We characterized the ligand-treated 3D perovskite thin films by XRD to confirm the formation of 2D structures. To increase the signal intensity for better characterization, the ligand solution (chlorobenzene/isopropanol) was dispensed on 3D thin films on a spin-coater and was allowed to stay for extended time before starting the spin-coating. As shown in **Figure 2**a, the characteristic peaks corresponding to 2D perovskites in the low angle region were observed in the 4TmI and 4TeI samples, while no characteristic 2D peaks appeared in the XRD pattern of 4TdmI sample. However, the existence of 4TdmI on the surface of perovskite thin film is evidenced through the X-Ray photoelectron spectroscopy (XPS) measurement (Fig. S11). The distortion of $[PbI_6]^{4-}$ when incorporating 4TdmI could potentially slow-down or prevent the formation of the 2D perovskite structure.

To better understand the 2D structure growth mechanism, the surface morphology evolution of the 3D perovskite thin films after treatment with the ligand solutions was analyzed using scanning electron microscopy (SEM). The ligand solutions were dispensed onto the 3D thin films and stayed for different amount of time before being spun off. Rectangular-shaped crystals on 3D thin film is apparent after 60 s of treatment with 4TmI solution as indicated in Figure 2d and S9, which are

designated as 2D crystals.[28–32] Enlarged crystals are observed when the reaction time is extended to 120 s (Figure 2e and S12). It is noteworthy that the 2D crystal can grow across the grain boundaries of 3D perovskite without breaking, indicating the 2D crystals are likely formed in an isolated free-standing manner, which suggests poor contact between 2D crystals and 3D surface. In contrast, no prominent 2D crystals can be observed in 4TeI-treated samples across the 120 s time span. Instead, the 4TeI-treated samples exhibit less obvious grain boundaries and more uniform surface morphology at 60 s and 120 s (Figure 2f-h and S13).

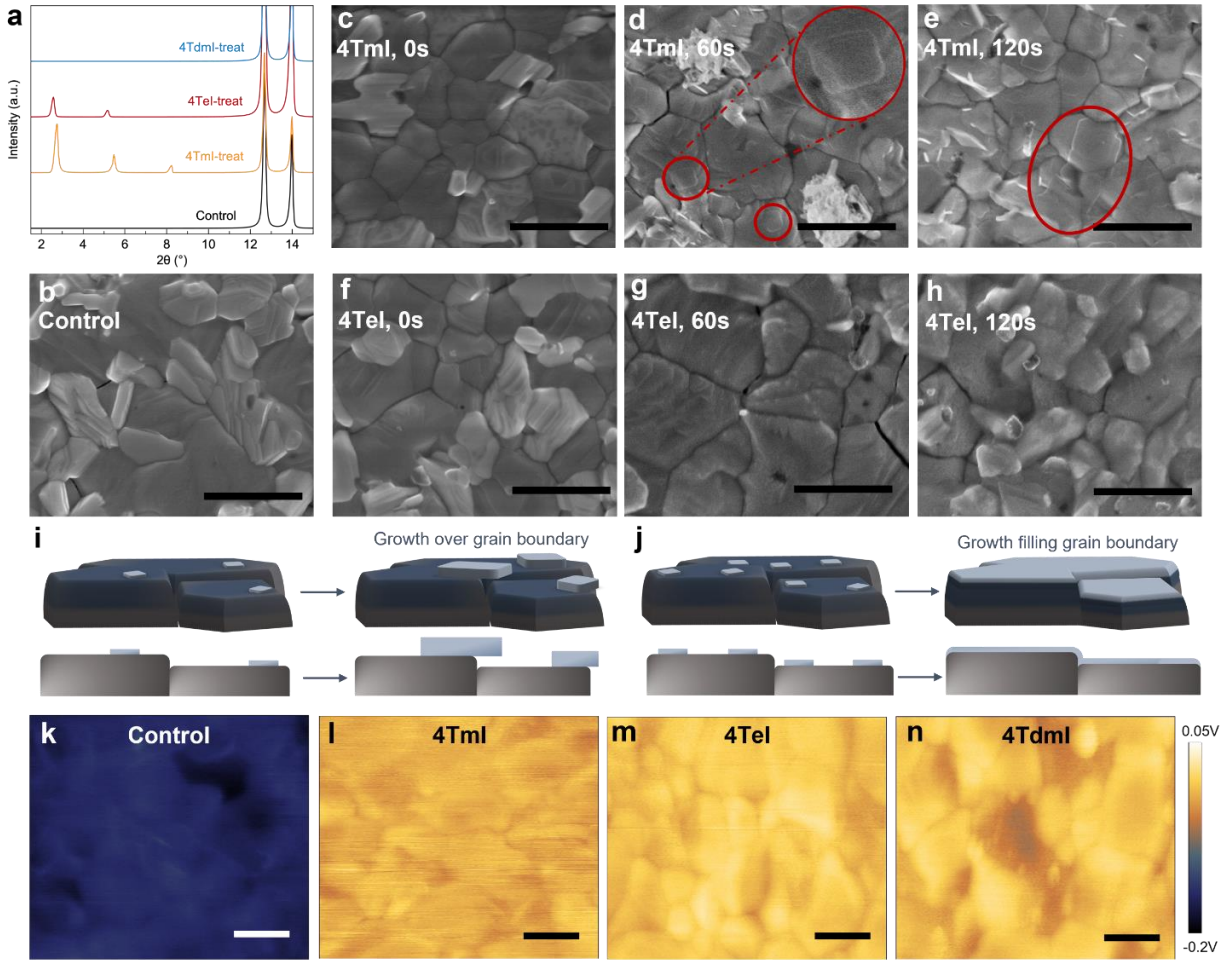

Figure 2. Surface property of passivated films a) XRD of perovskite thin films, passivated with different ligands, compared with control sample. b) SEM of bare perovskite thin films. c-e) SEM of perovskite thin films passivated with 4TmI, ligand solution stayed for 0 s, 60 s and 120 s before spin start. f-h) SEM of $FAPbI_3$ thin films passivated with 4TeI, ligand solution stayed for 0 s, 60 s and 120 s

before spin start, scale bar: 1 μm. i) Proposed 2D perovskite growth mechanism for 4TmI. j) Proposed 2D perovskite growth mechanism for 4TeI. k-m) Surface potential of perovskite thin films passivated without and with different ligands, scale bar: 1 μm.

2D structure formation was confirmed through their XRD patterns (Fig. S14), which suggest**s** the 2D/3D heterojunctions of 4TeI form in a different process compared with 4TmI samples (see below). In addition, the aggregation of ligands, observed in 4TmI samples (white cluster in SEM images), did not appear in 4TeI-treated samples, further evidencing the excellent solubility of 4TeI.

The interactions between ligands and the surface of 3D perovskite were further probed with XPS characterization. The S 2p signal at 164 eV in all the ligand-treated perovskite thin films confirmed the existence of the conjugated ligands, despite a short period of contact between 3D perovskite and the ligand solution (Figure. S11). The Pb 4f shows two main peaks at 138.2 eV and 143.1 eV for the control sample, corresponding to $4f_{7/2}$ and $4f_{5/2}$, respectively. While the surface treatment with 4TmI and 4TdmI did not change the Pb 4f signal, the 4TeI treatment shifted the Pb 4f peaks slightly towards low energy by 0.2 eV with minimal change in the work function. This peak shift could be correlated with the stronger interactions between 4Te and I^- in $[PbI_6]^{4-}$ octahedron and/or small changes in crystal structure.

According to the observation above, we hypothesize a growth mechanism of 2D/3D heterostructures with 4TmI and 4TeI as following (Figure 2i and 2j). Due to the relatively low solubility of 4TmI in chlorobenzene, the coverage of 4TmI on 3D perovskite is limited by diffusion and localized high concentration, and as a result having higher potential of generating non-uniform 2D structure. In addition, the stable 2D structure and low solubility of 4TmI+PbI_2 tend to cause the preferential growth of large free-standing crystals. In contrast, the high solubility of 4TeI in chlorobenzene and the strong interaction with PbI_2, all result in homogeneous distribution and increased amount of nucleation seeds. These properties likely help to ensure the full coverage of 2D structure on 3D surface. During the crystal growth process, the slightly larger strain of 4Te-based 2D lattice, which will be further confirmed with simulation, inhibits the growth of $(4Te)_2PbI_4$ into large hanging crystals, and substantially results in the conformal growth of 2D/3D heterostructure.

We further performed Kelvin probe force microscopy (KPFM) to ensure the full coverage of ligands on perovskite surface during the short time surface treatment (Figure 2k-2n). We observed that all the thin films with ligand treatment exhibit increased surface potential compared with the control film, which is correlated with decreased work functions. This relative homogeneous work function change indicates the full coverage of ligands on perovskite thin film surface even in the region without obvious morphology change (Figure S15).

2.3. Interfacial Adhesion and Molecular Interactions

Besides tuning the heterogeneity of 2D/3D heterostructures, the designed ligand molecules with hydrophobic quaterthiophene tails and hydrophilic ammonium head groups also strengthen the adhesion between hydrophobic polymeric hole transporting materials and hydrophilic halide perovskite materials. Here we used 4TeI as a representative ligand to investigate the interfacial strength change after surface treatment. The water contact angle with perovskite thin film increased from 63.4° to 82.3° after 4TeI treatment, suggesting the hydrophobicity of perovskite surface is enhanced (Figure S16), which could lead to better contact with the PTAA layers.

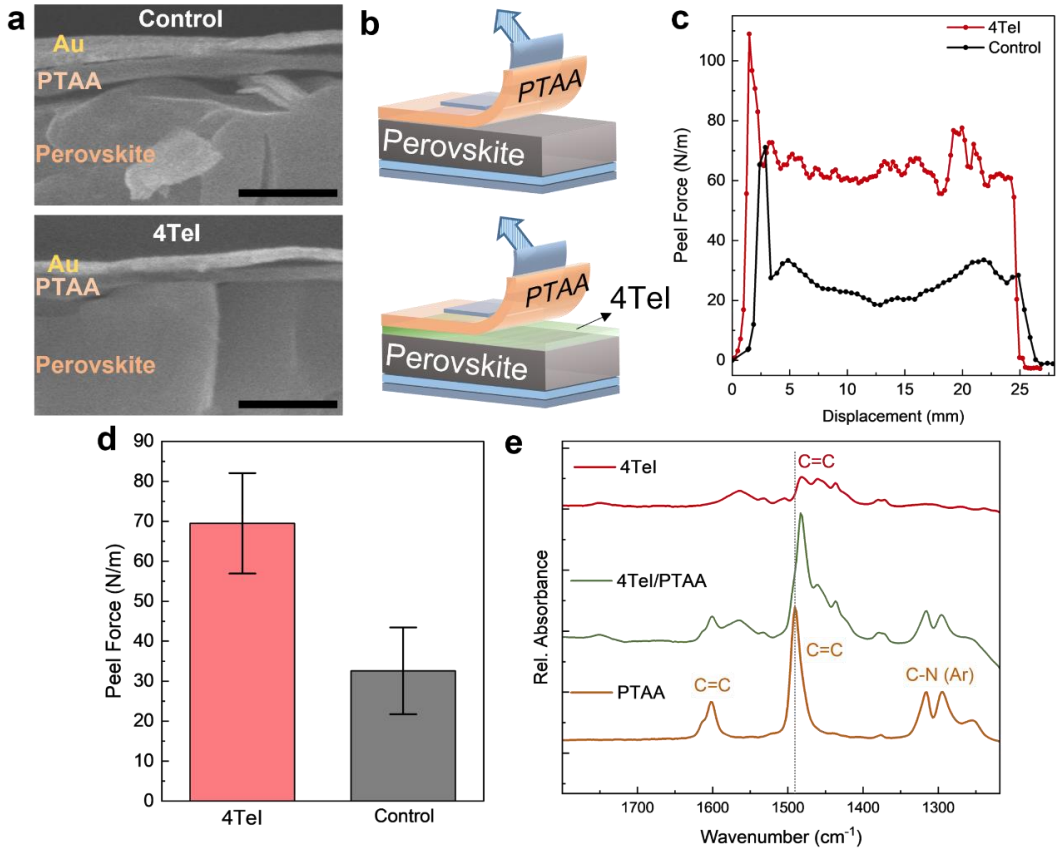

Figure 3. Interfacial adhesion a) Cross-section SEM of ITO/SnO_2/perovskite/PTAA/Au devices without (top) and with 4TeI (bottom) surface passivation, scale bar: 500 nm. b) Schematics of a peeling process for a pristine ITO/SnO_2/perovskite/PTAA thin film (top) and a ligand passivated thin film (bottom). c) 90° peel tests performed on perovskite/PTAA thin film samples with and without 4TeI passivation. d) The statistics of the peel force for 4TeI and control. Each condition is consisted of three samples. Error bars are representative standard deviation for each sample at center plateau region. e) Infrared absorption spectra of 4TeI, 4TeI/PTAA and PTAA on glass substrates. For 4TeI/PTAA samples, PTAA was spun-coated onto 4TeI.

Cross-sectional SEM images of control and 4TeI-treated devices (**Figure 3**a) also show that the PTAA layer binds tightly to the perovskite surface for 4TeI device, but relatively large gaps at the

perovskite/PTAA interface can be observed for the control device. Note that 2D layer is thin, thus not observable from cross-sectional SEM.

To further understand the adhesion at perovskite/PTAA interface, 90° peel tests were performed on ITO/SnO_2/perovskite/PTAA thin films with or without 4TeI treatment (Figure 3b-d).[27,33–35] Delamination failure occurred at the weakest interface, which was the perovskite/PTAA interface for both 4TeI-treated and control samples (Figure S17). However, with 4TeI surface treatment, the average peeling strength increased more than two-fold when compared with the control (without ligand passivation), from 32.6 N/m to 69.5 N/m. The result reveals that 4TeI molecule significantly enhances the interfacial adhesion between 3D perovskite layer and PTAA polymeric layer. The enhanced adhesion is primarily explained via the increased intermolecular interactions between the 4TeI and PTAA layers. To study the secondary interactions between 4TeI and PTAA, attenuated total reflectance-Fourier transform infrared spectroscopy (ATR-FTIR) was conducted (Figure 3e). PTAA shows symmetric C=C stretching at 1601 cm^{-1} and 1490 cm^{-1}, and aromatic C-N stretching at 1315 cm^{-1} and 1294 cm^{-1}.[36] 4TeI shows a series of C=C stretching between 1481 cm^{-1} and 1420 cm^{-1}.[37] Compared with the individual 4TeI and PTAA thin films, 4TeI/PTAA thin film (PTAA coated on top of 4TeI) shows that the C=C stretching of PTAA shifted to 1481 cm^{-1}, indicating the weaker C=C bond strength from π electrons in PTAA interacting with thiophenes. In addition, samples were also prepared via applying 4TeI on top of PTAA or premixing PTAA and 4TeI solution, similar frequency shift is observed, which is consistent with the current method (Figure S18).

Overall, the direct growth of a conformal 4TeI-2D layer atop of 3D perovskite, together with the hydrophobic π-π interaction with PTAA, illustrate the efficacy of our ligand passivation strategy on solving the interfacial contact problem between polymeric HTL and perovskite layers.

2.4. Carrier Dynamics and Device Performance

In addition to the geometric structure modulation, the ligand treatments also allow delicate control over electronic structure at 2D/3D heterojunctions. With the assistance of ultraviolet photoelectron spectroscopy (UPS), we analyzed the valence band maximum (VBM) and work function (WF) of

perovskite thin films (Figure S19 and Table S1). All the ligand-treated samples exhibit similar VBM (between −4.86 and −4.93 eV) and WF (between 3.75 and 3.82 eV), which are upshifted from the control sample with a VBM of -5.57 eV and a WF of 4.22 eV, and is due to the similar and shallow HOMO levels of the conjugated ligands. The significant shift in the WF for the 2D/3D heterojunctions is indicative of a large interfacial dipole at the 2D/3D heterojunction, as depicted in Figure S19. After forming the 2D/3D heterojunction, the VBM of the 3D phase is most closely aligned with the VBM of the 2D phase containing 4TeI, with a VBM offset of 0.31 eV for 4TmI, 0.24 eV for 4TdmI, and 0.17 eV for 4TeI. The aligned-VBMs indicate that all the 2D/3D heterojunctions form a type-II energy alignment that favors hole extraction, with the smaller VBM offset with 4TeI providing the most favorable energetics for hole extraction.

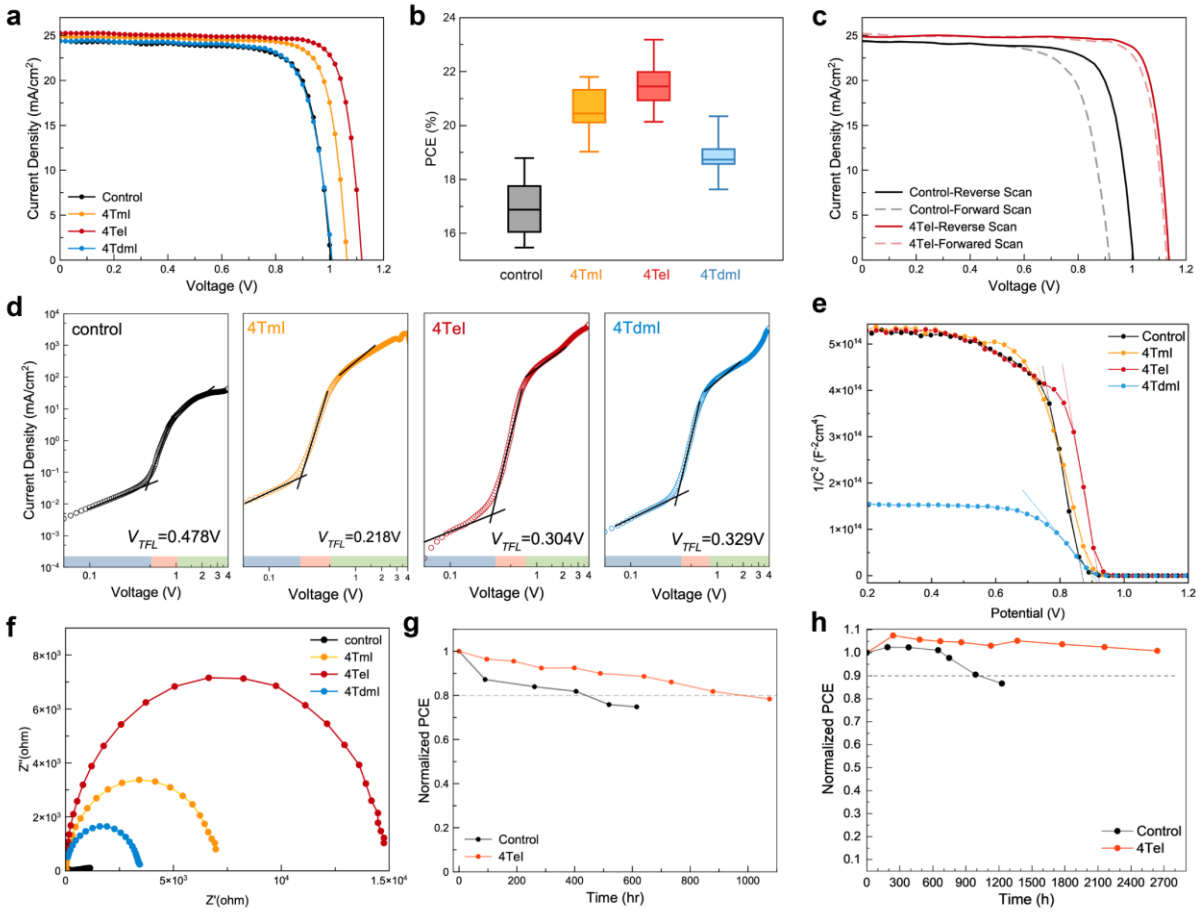

Figure 4. Device performance and characterization a) J-V curves of PSCs without passivation and with 4TmI, 4TeI, 4TdmI passivation under reverse scan. b) Statistics PCE of PSCs with different passivation. c) Reverse and forward scan of J-V curves of a 4TeI champion device and a control device (with MgF_2 coating). d) SCLC of hole-only devices. e) Mott-Schottky plots for control, 4TmI, 4TeI and 4TdmI devices. f) Nyquist plots for control, 4TmI, 4TeI and 4TdmI devices. g) 60°C thermal stability for reference and 4TeI devices. h) Moisture stability for reference and 4TeI devices in ambient condition, RH%= 56.1% ± 8.2%.

We prepared n-i-p (negative-intrinsic-positive) solar cell devices with different surface treatment and obtained a typical set of current density-voltage curves (**Figure 4**a). Compared to the control device, 4TdmI device shows no significant improvement due to the limited solubility and the lack of detectable 2D structures on top of 3D perovskites. In contrast, 4TeI-treatment significantly increases the efficiency, resulting a champion PCE of 23.7%, short-circuit current density (J_{SC}) of 24.9 mA cm^{-2}, fill factor (*FF*) of 83.8% and open-circuit voltage (V_{OC}) of 1.137 V (Figure 4b and 4c). The stabilized power output also gives an efficiency of 23.4%, together with the 24.6 mA cm^{-2} J_{SC} integrated from the external quantum efficiency (Figure. S20), confirming the high efficiency. Comparing to the 4TmI-device, 4TeI-device exhibits more enhancement in both *FF* and V_{OC}, which is mainly due to the synergistic effects of better energy alignment and conformal coating (Figure S21).

Space-charge limited current (SCLC) measurements were conducted on hole-only devices with a configuration of ITO/PEDOT:PSS/perovskite/ligand-2D/PTAA/Au (Figure 4d and Table S2). Unlike control device with a trap-filled limit voltage (V_{TFL}) at 0.478V, all the ligand passivated devices have smaller V_{TFL}, indicating the reduced defect density after passivation. Due to slightly strained structure, 4TeI has higher defect density than 4TmI. Derived from the trap-free SCLC region, the hole mobility of device with 4TeI-treatment was increased compared with control devices, as a consequence of suitable energy alignment and robust physical interfaces. The fitting results of space-charge capacitance via Mott-Schottky analysis determined the built-in potentials as 0.87 V, 0.90V, 0.92 V and 0.90 V for control, 4TmI-, 4TeI- and 4TdmI- devices, respectively, which agree with the trend of V_{OC} measured at 1 sun condition (Figure 4e). Electrochemical impedance spectroscopy

was applied to probe the charge transfer kinetics, and 4TeI reveals the highest charge recombination resistances in Nyquist plots (Figure 4f).

The conjugated ligand treatment strategy also applies to devices with other polymeric hole transporting materials, e.g., poly(3-hexylthiophene-2,5-diyl) (P3HT) and poly(N,N'-bis-4-butylphenyl-N,N'-bisphenyl)benzidine (poly-TPD) (Figure S22).[38–40] The HOMO of P3HT and Poly-TPD is −5.0 eV and −5.3 eV, respectively, aligned with the ligand-2D passivated VBM. Compared with control samples, 4TeI passivated devices showed enhanced PCE for both polymer HTLs. The consistent results further demonstrate that our ligand passivation strategy is an effective approach for improving the charge extraction and interfacial contact in majority of PSCs using polymer semiconducting materials as HTLs.

With better interfacial contact, improved charge transfer, and decreased defect density, the unencapsulated 4TeI devices show longer lifetime compared with control devices. At 60 °C heating condition in N_2 environment, 4TeI passivated device retained 80% of its initial efficiency for 1100 hours, while the reference device decreased to 70% after 500 hours (Figure 4g). Given the excellent water-soaking stability of 4TeI-2D perovskite thin films, we further investigated the moisture stability of 4TeI-2D passivated PSCs. In ambient condition, unencapsulated 4TeI devices retained up to 100% of the initial PCE after 2640 hours, whereas the reference devices decreased to 87% within 1228 hours (Figure 4h).

2.5. Structural Simulation and Ion Migration

To interrogate the crystal growth mechanism and ion migration in related with the stability of devices, we further performed MD simulations on ligand 2D perovskite structures (procedures for all the calculations are detailed in the SI). The stability of perovskite structure is quantified by I-Pb-I bond deviation ($\boldsymbol{\Delta\langle\lambda\rangle}$) and angle deviance ($\boldsymbol{\Delta\langle\sigma^2\rangle}$) from their ideal values (definitions detailed in the SI). Both 4Tm and 4Te 2D perovskites have bond deviation smaller than 0.005. However, 4Te sample exhibits an angle deviance of 46 degree^2, which is larger compared to the 36 degree^2 of 4Tm sample (**Figure 5**a and 5b). The larger angle deviance of 4Te sample is likely due to the additional strain

caused by the bulkier ethyl sidechain. From the top view of perovskite lattice, we also observed more ordered packing of 4Tm compared with that of 4Te (Figure 5c and 5d). The energy probability distribution function (PDF) of each ligand within the perovskite lattice was calculated to illustrate the extent of ordered packing (Figure 5e). 4Tm shows a narrower distribution than 4Te, which suggests 4Tm has a more ordered packing, arising from a slightly lower lattice strain in 4Tm 2D perovskite. We further performed the free energy calculation on the ligand rotation from breaking its equilibrated configuration within the perovskite lattice (Figure 5f and S23). Note that the unbiased equilibrated stacking angle of 4Tm is smaller (~20°) compared to that of 4Te (~50°), which suggests 4Tm has more parallel stacking initially. As the ligand broke from equilibrated stacking, 4Tm showed a steep increase in free energy as the rotation angle increased, with shallow local minima at ~40° and 60°, while the curve of 4Te increased more slowly with a local minimum at ~80°. Further examining the free energy change of 4Te exhibited that, by reverse rotating the ligand from its equilibrated angle of 50° to 0°, the curve showed a drastic increase, confirming 4Te prefers less parallelly stacked configuration due to steric repulsion. Combining PDF and free energy analysis, 4Te introduces slightly higher strain in 2D perovskite lattice, prefers lower extent of ordered packing and the packings are not subjected to one orientation. On the other hand, 4Tm prefers ordered packing without the tendency of configuration change. Therefore, the MD simulation results are consistent with our proposed 2D crystal growth mechanism which demonstrates that 4TmI can form large free-standing 2D perovskite crystals while 4TeI tends to generate conformal 2D coating and realize full coverage on the surface.

Besides the improved 2D coverage with efficient charge extraction (less charge accumulation) and lower defect density that lead to the enhanced stability, the excellent stability of 4TeI-treated devices can be further attributed to the relative high iodide anion migration energy barrier based on MD simulation results (Figure 5g, 5h and S23).[41] The anion migration was calculated within the inorganic layer (Figure 5g) and between the inner and the surface layer (Figure 5h). All the ligands exhibited free energy barrier higher than methylammonium (MA) (a standard barrier for 3D perovskite). Among all three ligands, 4Te shows the highest energy barrier at 0.8 eV, agreeing well with the superior experimental stability of 4TeI based PSCs.

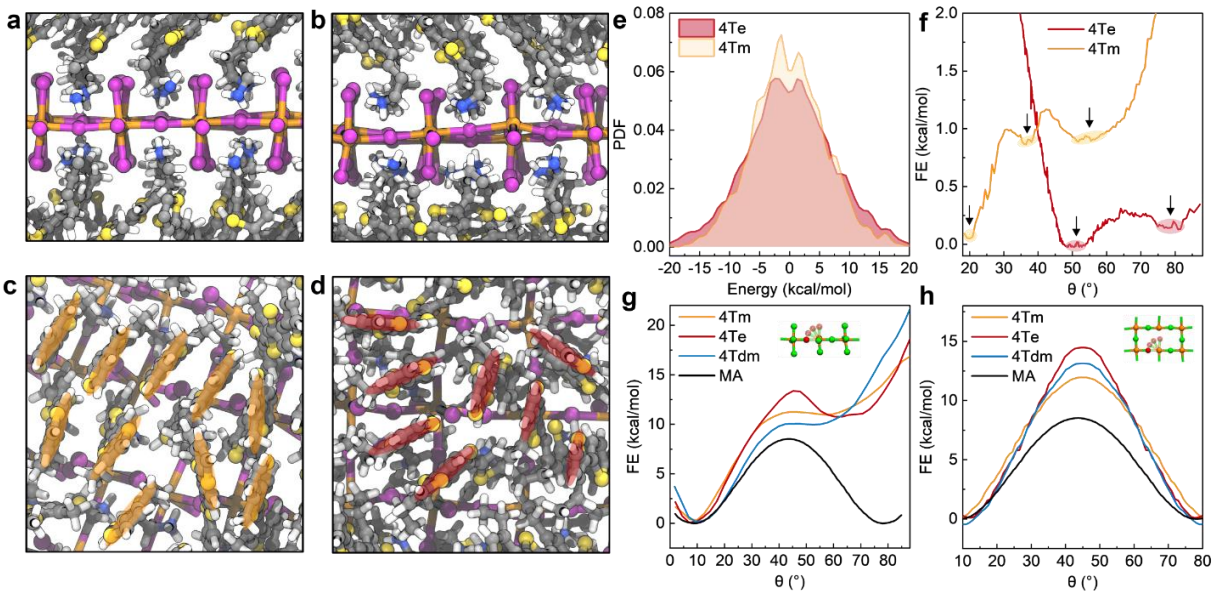

Figure 5. MD simulations on ligand packing in perovskite lattice a) Side view of 4Tm in perovskite lattice during unbias MD simulation. b) Side view of 4Te in perovskite lattice during unbias MD simulation. c) Top view of 4Tm in perovskite lattice, the orange lines denote the tail of the 4Tm. d) Top view of 4Te in perovskite lattice, the red lines denote the tail of the 4Te. e) The energy PDF of each ligand within the perovskite lattice. f) Free energy for neighboring ligand rotation within perovskite lattice, the arrow at ~20° for 4Tm and that at ~50° for 4Te denotes the initial ligand packing angle, respectively. g) Free energy (FE) barrier for ion migration between inner and surface layer and h) within inner layers.

3. Conclusion

We have synthesized a series of new thiophene-based conjugated ligands and quantified the optoelectronic properties of the as-formed organic-inorganic hybrid 2D perovskite. The ligands were further applied to 3D perovskite surface for the construction of 2D/3D heterostructure addressing the perovskite/polymeric HTL interfacial problems. On the 2D/3D interface, various side-chains introduced different lattice strains. Thus, two different 2D crystal growth mechanisms and surface morphology were revealed on the interface. On the 2D/PTAA hole transporting layer interface,

conformal 2D layers and intermolecular interaction between the ligands and PTAA enhanced the interfacial adhesion and thus ameliorated the poor wetting of PTAA on 3D perovskite. Devices fabricated with PTAA and the novel conjugated ligand, 4TeI, delivered the champion PCE of 23.7%, showing remarkable enhancement compared with control devices. PDF and free energy profile of 2D perovskites incorporating the new ligands deepen the understanding of 2D perovskite packing with different lattice strain and structural tunability. Lastly, with the high iodide migration energy barrier, our devices with 4TeI treatment demonstrated excellent thermal stability and moisture stability. Our molecular engineering approach is a general strategy that can be adapted to other polymeric hole-transporting materials, and we therefore proposed that future work can be targeting various interfaces, facilitated with tailored molecular design.

Supporting Information

Supporting Information is available from the Wiley Online Library or from the author.

Acknowledgements

J. S. and K. M. contributed equally to this work. This material is based upon work supported by the U.S. Department of Energy's Office of Energy Efficiency and Renewable Energy (EERE) under the Solar Energy Technologies Office Award DE-EE0009519. K.M. acknowledges the finial support from Lillian Gilbreth Postdoctoral Fellowships. D.J.L. acknowledges funding from the Air Force Office of Scientific Research (AFOSR) for supporting the adhesion measurements under award no. FA9550-22-1-0454. H.R.A. and K.R.G. acknowledge funding from the Office of Science of the U.S. Department of Energy for supporting the UPS and XPS measurements under award no. DE-SC0018208. The views expressed herein do not necessarily represent the views of the U.S. Department of Energy or the United States Government.

Conflict of Interest

The authors declare no conflict of interest.

Author Contributions

L.D., J.S. and K.M. conceived the research. J. S and D.V. did the organic synthesis; K.M. and J.S. developed the method for perovskite solar device fabrication. H.A. and K.R.G. performed UPS and XPS measurement and analysis. A.X.C. and D.J.L. conducted the adhesion measurements and analyzed the results. Z.L. and B.M.S. performed MD simulations; Y.T. and Y. L. performed SEM characterizations. K.M. performed KPFM and AFM measurements; all authors read and revised the manuscript

Received: ((will be filled in by the editorial staff))
Revised: ((will be filled in by the editorial staff))
Published online: ((will be filled in by the editorial staff))

References

[1] H. Min, D. Y. Lee, J. Kim, G. Kim, K. S. Lee, J. Kim, M. J. Paik, Y. K. Kim, K. S. Kim, M. G. Kim, T. J. Shin, S. Il Seok, *Nature* **2021**, *598*, 444.

[2] Y. Zhao, F. Ma, Z. Qu, S. Yu, T. Shen, H. X. Deng, X. Chu, X. Peng, Y. Yuan, X. Zhang, J. You, *Science* **2022**, *377*, 531.

[3] Y. Rong, Y. Hu, A. Mei, H. Tan, M. I. Saidaminov, S. Il Seok, M. D. McGehee, E. H. Sargent, H. Han, *Science* **2018**, *361*, 1214.

[4] M. A. Green, A. Ho-Baillie, H. J. Snaith, *Nat. Photonics* **2014**, *8*, 506.

[5] S. Kazim, M. K. Nazeeruddin, M. Grätzel, S. Ahmad, *Angew. Chemie - Int. Ed.* **2014**, *53*, 2812.

[6] M. Grätzel, *Acc. Chem. Res.* **2017**, *50*, 487.

[7] C. Liang, H. Gu, Y. Xia, Z. Wang, X. Liu, J. Xia, S. Zuo, Y. Hu, X. Gao, W. Hui, L. Chao, T. Niu, M. Fang, H. Lu, H. Dong, H. Yu, S. Chen, X. Ran, L. Song, B. Li, J. Zhang, Y. Peng, G. Shao, J. Wang, Y. Chen, G. Xing, W. Huang, *Nat. Energy* **2021**, *6*, 38.

[8] Y. W. Jang, S. Lee, K. M. Yeom, K. Jeong, K. Choi, M. Choi, J. H. Noh, *Nat. Energy* **2021**, *6*, 63.

[9] W. S. Yang, B. W. Park, E. H. Jung, N. J. Jeon, Y. C. Kim, D. U. Lee, S. S. Shin, J. Seo, E. K. Kim, J. H. Noh, S. Il Seok, *Science* **2017**, *356*, 1376.

[10] N. Yaghoobi Nia, M. Méndez, B. Paci, A. Generosi, A. Di Carlo, E. Palomares, *ACS Appl. Energy Mater.* **2020**, *3*, 6853.

[11] Y. Kim, E. H. Jung, G. Kim, D. Kim, B. J. Kim, J. Seo, *Adv. Energy Mater.* **2018**, *8*, 1801668.

[12] W. S. Yang, J. H. Noh, N. J. Jeon, Y. C. Kim, S. Ryu, J. Seo, S. Il Seok, *Science* **2015**, *348*, 1234.

[13] S. Song, E. Y. Park, B. S. Ma, D. J. Kim, H. H. Park, Y. Y. Kim, S. S. Shin, N. J. Jeon, T. S. Kim, J. Seo, *Adv. Energy Mater.* **2021**, *11*, 2003382.

[14] T. Y. Yang, N. J. Jeon, H. W. Shin, S. S. Shin, Y. Y. Kim, J. Seo, *Adv. Sci.* **2019**, *6*, 1900528.

[15] Y. Wang, L. Duan, M. Zhang, Z. Hameiri, X. Liu, Y. Bai, X. Hao, *Sol. RRL* **2022**, *6*, 2200234.

[16] F. M. Rombach, S. A. Haque, T. J. Macdonald, *Energy Environ. Sci.* **2021**, *14*, 5161.

[17] R. Azmi, E. Ugur, A. Seitkhan, F. Aljamaan, A. S. Subbiah, J. Liu, G. T. Harrison, M. I. Nugraha, M. K. Eswaran, M. Babics, Y. Chen, F. Xu, T. G. Allen, A. Rehman, C. Wang, T. D. Anthopoulos, U. Schwingenschlögl, M. De Bastiani, E. Aydin, S. De Wolf, *Science* **2022**, *5784*, 73.

[18] S. Sidhik, Y. Wang, M. De Siena, R. Asadpour, A. J. Torma, T. Terlier, K. Ho, W. Li, A. B. Puthirath, X. Shuai, A. Agrawal, B. Traore, M. Jones, R. Giridharagopal, P. M. Ajayan, J. Strzalka, D. S. Ginger, C. Katan, M. A. Alam, J. Even, M. G. Kanatzidis, A. D. Mohite, *Science* **2022**, *377*, 1425.

[19] K. Ma, H. R. Atapattu, Q. Zhao, Y. Gao, B. P. Finkenauer, K. Wang, K. Chen, S. M. Park, A. H. Coffey, C. Zhu, L. Huang, K. R. Graham, J. Mei, L. Dou, *Adv. Mater.* **2021**, *33*, 2100791.

[20] J. Xue, R. Wang, X. Chen, C. Yao, X. Jin, K. L. Wang, W. Huang, T. Huang, Y. Zhao, Y. Zhai, D. Meng, S. Tan, R. Liu, Z. K. Wang, C. Zhu, K. Zhu, M. C. Beard, Y. Yan, Y. Yang, *Science* **2021**, *371*, 636.

[21] G. Yang, Z. Ren, K. Liu, M. Qin, W. Deng, H. Zhang, H. Wang, J. Liang, F. Ye, Q. Liang, H. Yin, Y. Chen, Y. Zhuang, S. Li, B. Gao, J. Wang, T. Shi, X. Wang, X. Lu, H. Wu, J. Hou, D. Lei, S. K. So, Y. Yang, G. Fang, G. Li, *Nat. Photonics* **2021**, *15*, 681.

[22] A. H. Proppe, A. Johnston, S. Teale, A. Mahata, R. Quintero-Bermudez, E. H. Jung, L. Grater, T. Cui, T. Filleter, C. Y. Kim, S. O. Kelley, F. De Angelis, E. H. Sargent, *Nat. Commun.* **2021**, *12*, 3472.

[23] G. Wu, R. Liang, M. Ge, G. Sun, Y. Zhang, G. Xing, *Adv. Mater.* **2022**, *34*, 2105635.

[24] Q. Jiang, Y. Zhao, X. Zhang, X. Yang, Y. Chen, Z. Chu, Q. Ye, X. Li, Z. Yin, J. You, *Nat. Photonics* **2019**, *13*, 460.

[25] M. Gutwald, N. Rolston, A. D. Printz, O. Zhao, H. Elmaraghi, Y. Ding, J. Zhang, R. H. Dauskardt, *Sol. Energy Mater. Sol. Cells* **2020**, *209*, 110433.

[26] J. Dou, Q. Song, Y. Ma, H. Wang, G. Yuan, X. Wei, X. Niu, S. Ma, X. Yang, J. Dou, S. Liu, H. Zhou, C. Zhu, Y. Chen, Y. Li, Y. Bai, Q. Chen, *J. Energy Chem.* **2023**, *76*, 288.

[27] Z. Dai, S. K. Yadavalli, M. Chen, A. Abbaspourtamijani, Y. Qi, N. P. Padture, *Science* **2021**, *372*, 618.

[28] Y. Gao, E. Shi, S. Deng, S. B. Shiring, J. M. Snaider, C. Liang, B. Yuan, R. Song, S. M. Janke, A. Liebman-Peláez, P. Yoo, M. Zeller, B. W. Boudouris, P. Liao, C. Zhu, V. Blum, Y. Yu, B. M. Savoie, L. Huang, L. Dou, *Nat. Chem.* **2019**, *11*, 1151.

[29] E. Shi, B. Yuan, S. B. Shiring, Y. Gao, Akriti, Y. Guo, C. Su, M. Lai, P. Yang, J. Kong, B. M. Savoie, Y. Yu, L. Dou, *Nature* **2020**, *580*, 614.

[30] L. Dou, A. B. Wong, Y. Yu, M. Lai, N. Kornienko, S. W. Eaton, A. Fu, C. G. Bischak, J. Ma, T. Ding, N. S. Ginsberg, L. W. Wang, A. P. Alivisatos, P. Yang, *Science* **2015**, *349*, 1518.

[31] D. Ma, Y. Fu, L. Dang, J. Zhai, I. A. Guzei, S. Jin, *Nano Res.* **2017**, *10*, 2117.

[32] C. R. Roy, D. Pan, Y. Wang, M. P. Hautzinger, Y. Zhao, J. C. Wright, Z. Zhu, S. Jin, *J. Am. Chem. Soc.* **2021**, *143*, 5212.

[33] A. X. Chen, J. D. Hilgar, A. A. Samoylov, S. S. Pazhankave, J. A. Bunch, K. Choudhary, G. L. Esparza, A. Lim, X. Luo, H. Chen, R. Runser, I. McCulloch, J. Mei, C. Hoover, A. D. Printz, N. A. Romero, D. J. Lipomi, *Adv. Mater. Interfaces* **2022**, *2202053*, DOI 10.1002/admi.202202053.

[34] R. Blau, A. X. Chen, B. Polat, L. L. Becerra, R. Runser, B. Zamanimeymian, K. Choudhary, D. J. Lipomi, *ACS Appl. Mater. Interfaces* **2022**, *14*, 4823.

[35] M. Dailey, Y. Li, A. D. Printz, *ACS Omega* **2021**, *6*, 30214.

[36] Y. Liu, Z. Liu, E. C. Lee, *ACS Appl. Energy Mater.* **2019**, *2*, 1932.

[37] A. Tamanai, S. Beck, A. Pucci, *Displays* **2013**, *34*, 399.

[38] D. Xu, Z. Gong, Y. Jiang, Y. Feng, Z. Wang, X. Gao, X. Lu, G. Zhou, J. M. Liu, J. Gao, *Nat. Commun.* **2022**, *13*, 7020.

[39] Y. Hou, X. Du, S. Scheiner, D. P. McMeekin, Z. Wang, N. Li, M. S. Killian, H. Chen, M. Richter, I. Levchuk, N. Schrenker, E. Spiecker, T. Stubhan, N. A. Luechinger, A. Hirsch, P. Schmuki, H. P. Steinrück, R. H. Fink, M. Halik, H. J. Snaith, C. J. Brabec, *Science* **2017**, *358*, 1192.

[40] Y. Sha, E. Bi, Y. Zhang, P. Ru, W. Kong, P. Zhang, X. Yang, H. Chen, L. Han, *Adv. Energy Mater.* **2021**, *11*, 2003301.

[41] Akriti, S. Zhang, Z. Y. Lin, E. Shi, B. P. Finkenauer, Y. Gao, A. J. Pistone, K. Ma, B. M. Savoie, L. Dou, *Adv. Mater.* **2021**, *33*, 2105183.

With tailored conjugated ligand design, the 2D/3D heterostructure built in perovskite solar cells enhances the interface adhesion between polymeric hole transporting layer—PTAA and perovskite,

and at the same time, realizes a uniform growth of 2D structure on top of 3D perovskite. Therefore, the as-fabricated device yields a 23.7% power conversion efficiency, along with excellent stability.

Jiaonan Sun[†], Ke Ma[†], Zih-Yu Lin, Yuanhao Tang, Dharini Varadharajan, Alexander X. Chen, Harindi R. Atapattu, Yoon Ho Lee, Ke Chen, Bryan W. Boudouris, Kenneth R. Graham, Darren J. Lipomi, Jianguo Mei*, Brett M. Savoie*, Letian Dou*

Tailoring Molecular-Scale Contact at Perovskite/Polymeric Hole Transporting Material Interface for Efficient Solar Cells